# Development of in-situ trap characterisation techniques for EMCCDs

## Journal Item

## oro.open.ac.uk

# Development of in-situ trap characterisation techniques for EMCCDs

**Nathan Bush,**[a] **David Hall,**[a] **Andrew Holland,**[a] **Ross Burgon,**[a] **Doug Jordan,**[b] **Patrick Morrissey,**[c] **Richard Demers,**[c] **Leon K. Harding,**[c] **Bijan Nemati,**[c] **Robert Effinger and**[c] **Michael Bottom**[c]

[a]*Centre for Electronic Imaging, The Open University, Walton Hall, Milton Keynes, MK7 6AA, UK*

[b]*Teledyne e2v technologies (UK) plc, 106 Waterhouse Lane, Chelmsford, Essex, CM1 2QU, UK*

[c]*Jet Propulsion Laboratory, California Institute of Technology, 4800 Oak Grove Drive, Pasadena, 91109, CA, USA*

*E-mail:* nathan.bush@open.ac.uk

ABSTRACT: The "trap pumping" technique has seen considerable use over recent years as a means to probe the intrinsic properties of silicon defects that can impact charge transfer performance within CCD-based technologies. While the theory behind the technique is reasonably well understood, it has to date only been applied to relatively simple pixel designs where the motion of charge between pixel phases is fairly easy to predict. For some devices, the intrinsic pixel architecture is more complex and can consist of unequal phase sizes and additional implants that deform the electronic potential. Here, we present the implementation of the trap pumping technique for the CCD201-20, a 2-phase Teledyne e2v EMCCD. Clocking schemes are presented that can provide the location of silicon defects to sub-micron resolution. Experimental techniques that allow determination of trap energy levels and emission cross sections are presented. These are then implemented on an irradiated CCD201-20 to determine the energy level and emission cross section for defects thought to be the double acceptor state of the silicon divacancy ($VV^{--}$) and carbon-phosphorus ($C_iP_s$) pairs. An improvement in charge transfer performance through optimised parallel clock delay is demonstrated and found to correlate with the properties of defects found using the trap pumping technique.

KEYWORDS: CCD, EMCCD, radiation damage, silicon defects, divacancy, trap pumping

---

[1]Corresponding author.

## Contents

## 1 Characterisation of radiation-induced traps within CCD based technologies

Operation of a CCD within a radiation environment gives rise to stable defects within the buried channel that increase Charge Transfer Inefficiency (CTI) and can limit the operational lifetime of the device [1, 2]. For space-based applications, considerable effort is therefore spent on minimising the impact of radiation damage through techniques such as optimised clocking [3, 4] and charge loss correction [5–9]. While these techniques have been successful in significantly reducing the impact of the damage, they can benefit further from more precise knowledge of the properties of defects responsible for charge loss [10]. "Trap pumping" is a technique that has been demonstrated to provide a high level of detail on individual defects responsible for charge loss. Prior to the introduction of the technique, the properties of silicon defects within CCDs were typically inferred from measurements of CTI as a function of temperature (e.g. [11] and [12]). While such techniques remain useful, they typically provide the average properties of one or more trap species as opposed to information on single lattice defects that trap pumping can provide. A detailed description of the development of the theory can be found within [10, 13, 14], and implementation examples found within [15, 16], therefore only a brief overview is presented here. The technique involves a flat field of illumination being clocked between phases within a pixel such that charge can be repeatedly captured by a trapping site and then emitted into a neighbouring pixel. Each step of the clocking scheme is separated by a controllable time, referred to here as the phase time ($t_{ph}$), that is typically constant for each step in the scheme. If a trap is present with an emission time constant ($\tau_e$) comparable to the phase time, charge may be "pumped" from one pixel to another. The repetition of this process over numerous cycles (typically $\geq 10^3$) gives rise to a bright-dark pixel pattern referred to as a "Dipole", shown in Figure 1. The dark pixel typically, but not always, represents the physical location of the trap (at pixel-level resolution) whereas the bright pixel is due
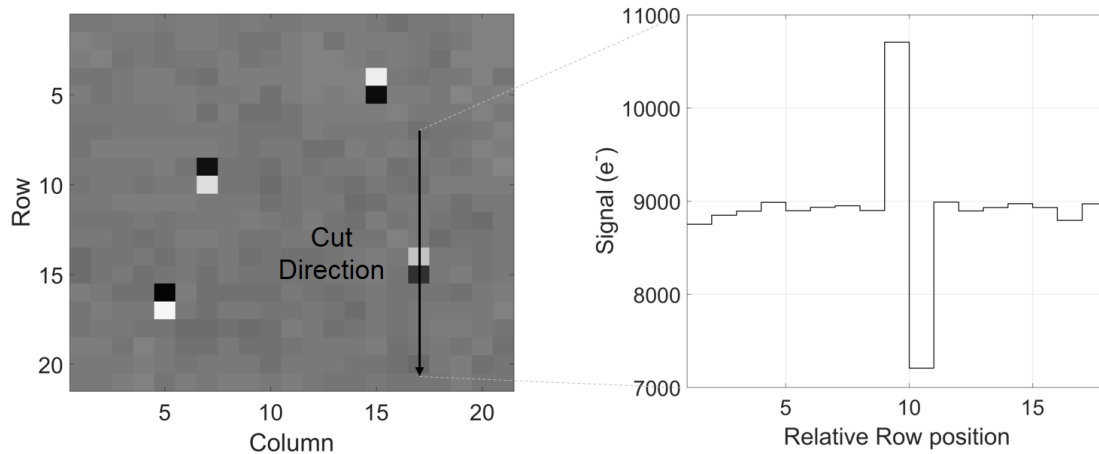
**Figure 1**. Left: A 'trap pumped' CCD image with dipoles highlighting the presence of silicon defects at pixel level resolution. Right: Signal profile of a dipole highlighting the characteristic bright-dark pattern whereby signal has been shifted from the background into a neighbouring pixel due to the repeated capture and emission of charge from a defect.

to charge that has been repeatedly captured and released into the neighbouring pixel, adding to the background signal level.

Measurements of the intensity (or amplitude) of the dipole at a given temperature as a function of the phase time ($t_{ph}$) give rise to an intensity curve of the form:

$$I(t_{ph}) = N P_P \tag{1.1}$$

Where $N$ is the number of pumping cycles and $P_p$ is the probability that a trap will pump within a complete clocking cycle. The probability that a trap will pump ($P_p$) requires the knowledge of how trapped charge will move under a specific set of clocking conditions. It therefore varies according to the pixel architecture of the device under study and the clocking scheme applied to said device. For a standard, 3-phase CCD pixel with electrodes of equal width, this movement is fairly straightforward to predict. However, unequal phase widths and additional implants distort the potential profile, making $P_p$ non-trivial and complicating the extraction of defect properties. Modern scientific CCDs make use of more complicated pixel designs to maximise performance. One example is the Teledyne e2v EMCCD, for which the standard variant has features to facilitate high speed, 2-phase clocking in Inverted Mode Operation (IMO). The EMCCD is being considered for use in photon counting applications where the impact of radiation induced trapping sites is expected to be significant [17, 18]. The development of the trap pumping technique for these devices therefore has the potential to inform modes of operation that significantly improve performance in the presence of radiation induced damage.

## 2 EMCCD technology and the CCD201 image pixel

For this study, we have applied the technique to the CCD201-20 EMCCD (hereafter, CCD201), although the same principles described here apply to any pixel with similar structure. The CCD201
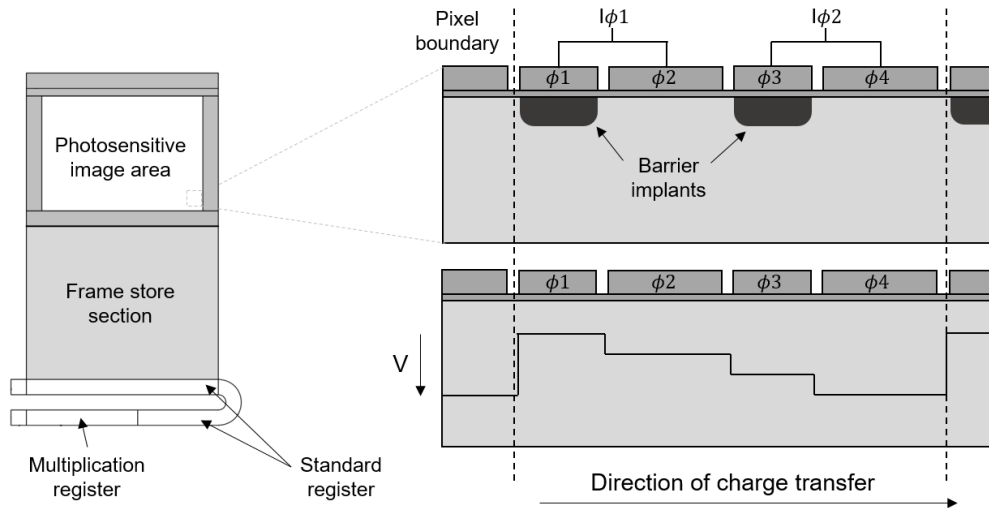
**Figure 2**. Left: Structure of an EMCCD with image area, standard register and multiplication register (A more comprehensive description can be found in [19] and [20]). Right: Schematic of an EMCCD image pixel, showing the barrier implants responsible for the "2-phase" clocking structure. The bottom panel shows the approximate potential profile within a pixel when $I\phi_1$ is held low and $I\phi_2$ is held high, hereafter referred to as "standard clocking conditions".

image pixel is 13 $\mu$m square, with four separately connected electrodes that can be paired to operate with 2-phase clocking in IMO if required (Figure 2). Two of the phases are larger in size and are where charge is stored during frame integration and clocking. They are hereafter referred to as "storage phases". The remaining two phases are smaller in size and feature an additional P implant that prevents the back-flow of charge during standard clocking. They are hereafter referred to as "barrier phases". The standard clocking conditions of the pixel are such that $\phi_1$, $\phi_2$ and $\phi_3$, $\phi_4$ are paired to give $I\phi_1$ and $I\phi_2$, respectively (Figure 2). Either $I\phi_1$ or $I\phi_2$ are powered at any one time and this gives rise to an asymmetric potential structure that not only prevents the back-flow of charge, but also promotes any captured charge to re-emit into the original signal packet. The 2-phase pixel design described here therefore provides an intrinsic potential structure that bears strong similarity to clock levels recommended in other studies for improved CTE and low Clock Induced Charge (CIC) [3]. The schematic shown in Figure 2, however, is only indicative - the exact potential profile must be known in order to predict the motion of trapped charge at all points within the pixel. TCAD simulation offers the capability to provide such information, and so was the starting point for the design of the EMCCD trap pumping schemes.

## 3 TCAD simulation of the CCD201 image pixel

The CCD201 image area pixel was constructed within a commercial TCAD software package (SILVACO ©[21]) so that the potential profiles could be used to design EMCCD trap pumping schemes. All parameters relating to the manufacturing of the pixel were accurately simulated, including ion implantation, fully-coupled dopant diffusion and polysilicon deposition processes. The geometry of the pixel was set to standard Teledyne e2v design parameters, including the
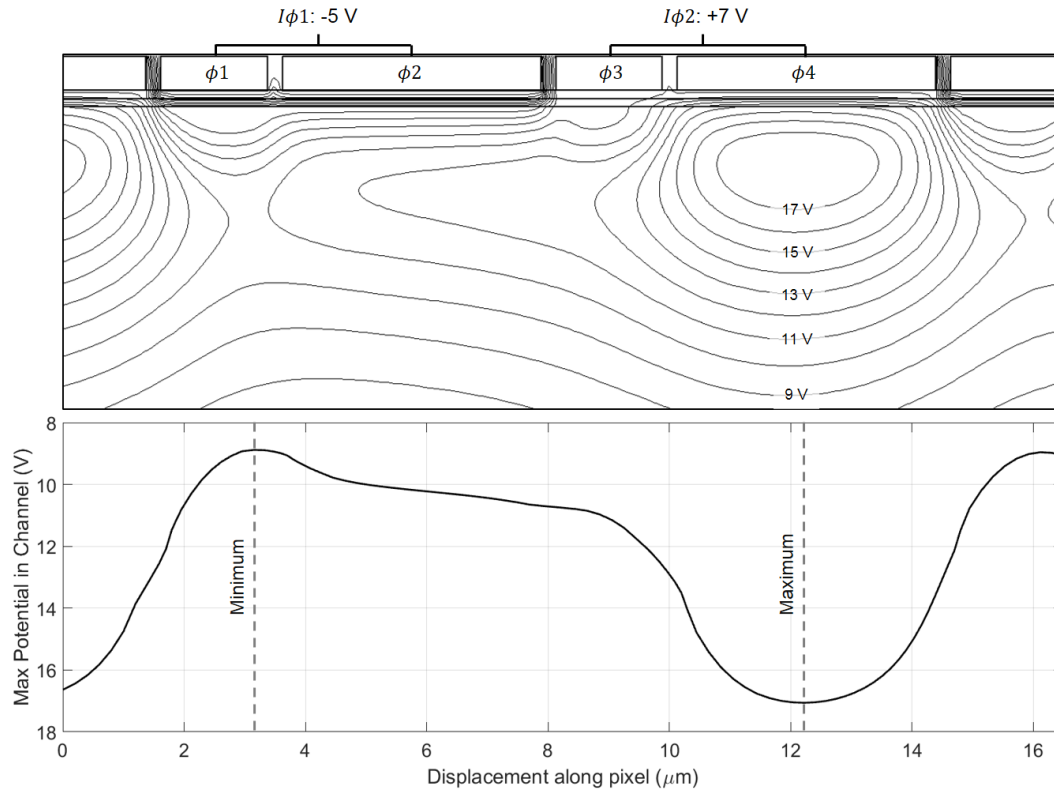
**Figure 3**. SILVACO TCAD simulation of a CCD201 image pixel operating at datasheet voltages in 2-phase Inverted Mode (IMO) [22]. In this example, both $\phi_1$ and $\phi_2$ are biased to the low state of -5 V and $\phi_3$ and $\phi_4$ are biased to the high state of + 7 V. Dashed lines indicate the location of the potential maximum and minimum.

sizes of each phase and the width of dielectric layers. Implantation doses were set such that each pixel had performance characteristics consistent with Teledyne e2v specifications, including the channel parameter ($\phi_{CH}$) and barrier phases of the image pixel. Following process simulation, the electronic characteristics of the pixel were simulated using Teledyne e2v datasheet values and any bias configurations required for the trap pumping schemes [22].

Figure 3 shows a 2D slice of a TCAD simulation of the CCD201 image pixel under standard clocking conditions ($I\phi_1$ held low and $I\phi_2$ held high). The potential profile within the bottom panel is similar to the schematic shown in Figure 2, bar a few notable differences. Most important are the locations of the potential minimum and maximum, since these dictate the effective pixel boundary and charge storage location respectively. The potential minimum is located beneath the barrier phase in the low state ($\phi_1$ in the example of Figure 3) and is not central beneath the phase but rather shifted towards $\phi_2$. The location of this minimum varied according to the bias levels to the adjacent storage phases, however the exact location was deemed insignificant for most purposes. Of more importance is the location of the potential maximum, and hence charge storage location, since this impacts the volume of silicon available for charge capture during the trap pumping process.

For standard pixel voltages [22], the potential maximum was found to shift by approximately 0.5 $\mu$m dependent upon the adjacent barrier phase that was held high (either $\phi_3$ or $\phi_1$). Figure 4
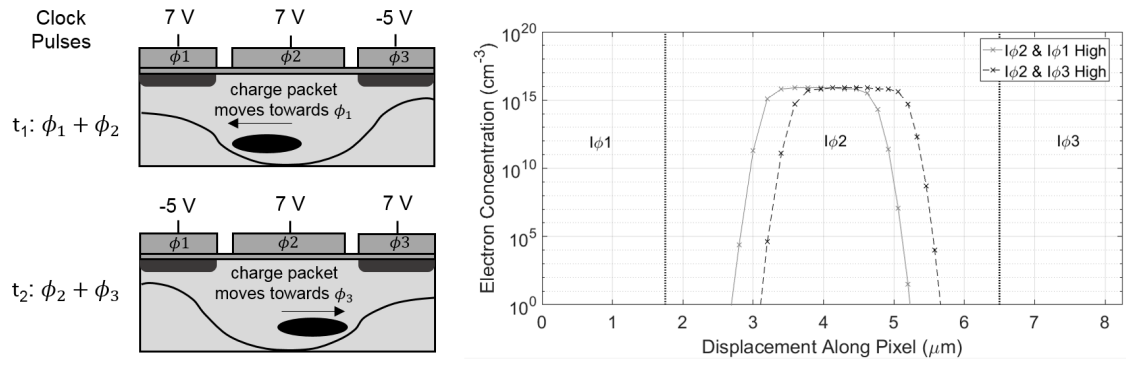
**Figure 4**. Left: Movement of charge depending upon how the adjacent barrier phase is biased. Right: TCAD simulation of an 10,000 e⁻ packet in the presence of the two bias configurations shown on the left panel. A 1D cut was taken through the centre of the packet.

shows the effect, where the charge cloud beneath a storage phase moves according to the adjacent barrier phase that is held high. The exact location of the maximum could be moved by changing the bias to the adjacent storage phases from the nominal value (+12 V relative to low level) to lower levels (+10 V, +9 V etc.). Thus, careful adjustment of the bias to an adjacent barrier phase allows one to "scan" the charge packet through this portion of the silicon to provide high resolution location information for trapping sites beneath the storage phases. It is the fact that the maximum shifts in this way, depending on the bias configuration, that gives rise to the sub-phase, sub-micron resolution for trap identification that will later be explored further.

A common assumption within a trap pumping routine is that the time taken for charge to transfer between phases is small compared to the dwell time beneath a given phase. When this assumption is met, charge capture does not occur beneath the barrier phases or inter-phase regions and a single function for $P_P$ is valid for as much of the pixel as possible. To validate this assumption for the CCD201, a simulation of charge transfer was performed within an image pixel using with a signal of 10,000 e⁻. Standard datasheet voltages were used in the simulation alongside clock rise time of 100 ns [22]. The models that handled the charge transfer process were the same as those used in [23] and are well validated [21]. The bottom panel of Figure 5 shows the charge measured beneath each of the storage phases as a function of time throughout the transfer. The vast majority of the signal is transferred between the phases within approximately 10 ns for these clocking conditions. The maximum charge density recorded in the region was $10^{14}$ e⁻/cm³, shown by the top panel of Figure 5. The middle panel of Figure 5 shows the resulting capture probability at the end of the transfer for this signal size and clocking conditions, where charge capture between the two storage phases is shown to be negligible. It should be noted that the use of either longer rise times or very large signals where transfer begins to become diffusion limited may cause this assumption to break down. The conclusion is that the 2-phase architecture of these devices does not facilitate significant charge capture beneath the barrier phases or inter-phase regions within the recommended range of bias levels. Trap pumping schemes therefore only need to consider the case of charge capture beneath the storage phases of the device.
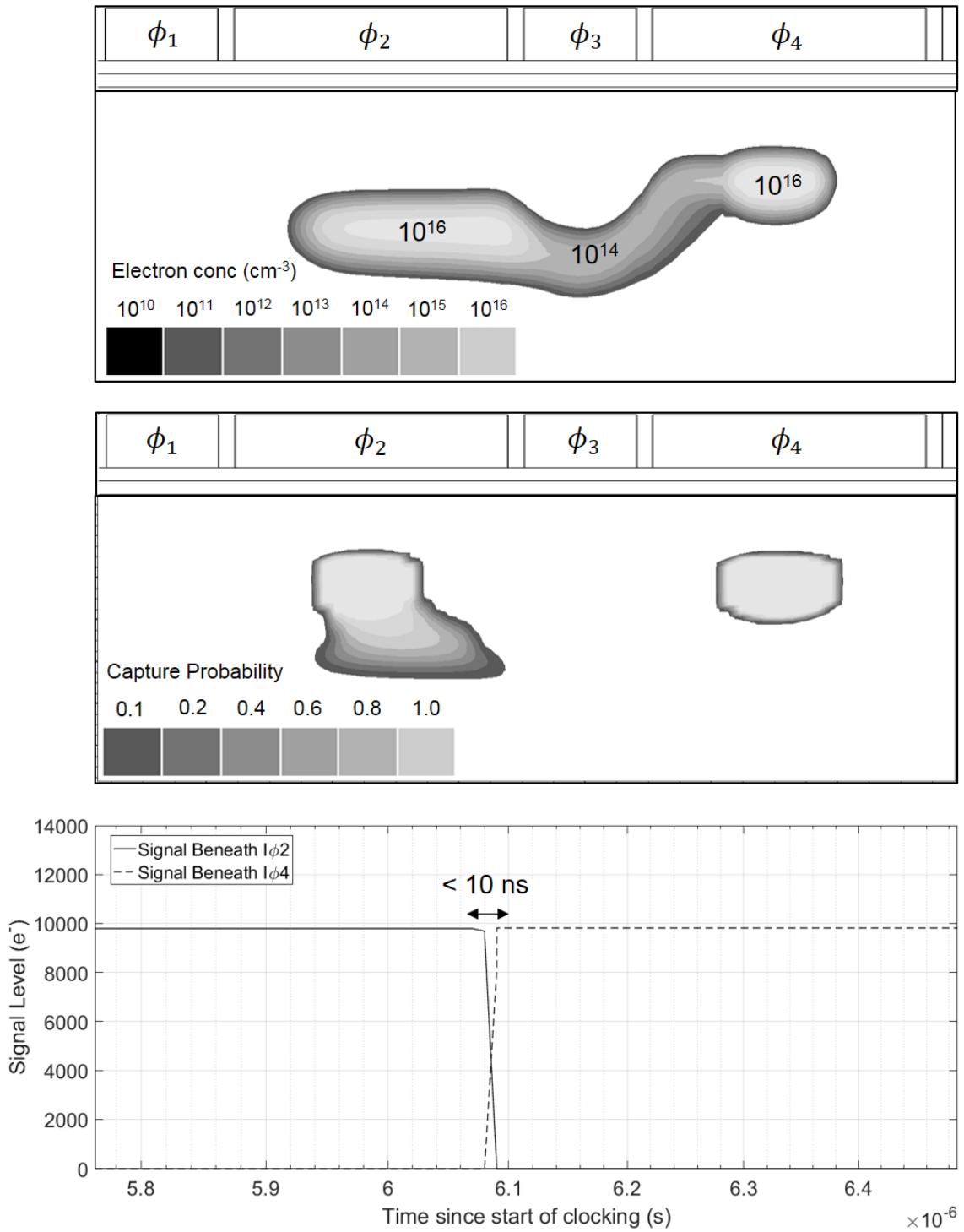
**Figure 5**. Simulation of charge transfer of 10000 e$^-$ within a CCD201 image pixel. The top panel shows a "snapshot" partway through the simulation. The maximum recorded charge density beneath the barrier phase was two orders of magnitude below that measured beneath the storage phases. The middle panel shows the fraction of filled traps at the end of the transfer process for defects with properties consistent with the VV$^{--}$ [10]. The bottom panel shows the charge recorded beneath $\phi_2$ and $\phi_4$ throughout the transfer. It can be seen that for these transfer conditions, no traps are filled beneath $\phi_3$, however this may change for the transfer of larger signal levels or the use of longer rise times (100 ns used in this simulation).

## 4 An example EMCCD trap pumping scheme

The simulations presented in the previous section provided both the potential profiles needed to predict the movement of charge and also validated the necessary assumptions required for the accurate extraction of trap properties. This allowed trap pumping schemes to be designed and implemented for the 2-phase CCD201. An example trap pumping scheme is presented by Figure 6. A total of four separate clock pulses are required for a complete cycle before the process repeats, each separated by a single phase time $t_{ph}$. Note how the conditions for successful trap pumping are satisfied; trapping sites can be filled beneath either of the storage phases and are then able to emit charge to the neighbouring pixel.

An example is shown on the diagram where a trap is present beneath the centre of $\phi_2$. During the first clock cycle, the trap becomes filled, since in the presence of high charge density ($\approx 10^{16}$ e$^-$/cm$^3$), the capture probability (P$_C$) approaches 1 for phase times ($t_{ph}$) longer than 100 ns. In the second step, the trap remains filled since it is still in the presence of the charge packet. If the trap emits in the third step then the charge will rejoin the original signal packet. No net motion of charge will occur and so emission during this time does not act to pump the trap. In the fourth step, the trap may emit and charge will be collected in the neighbouring pixel. If the scheme is performed over multiple cycles in the presence of this trap, the signal level within the primary pixel will decrease while the signal in the neighbouring pixel will increase, giving rise to a dipole as shown by Figure 1. The corresponding function of P$_P$ for $\phi_2$ is therefore given by the probability that the trap will emit charge during step 4.

For the example of $\phi_2$, emitted charge pumps against the direction of transfer. Charge captured beneath $\phi_4$, however, will pump along the direction of transfer. The phase location of the defect therefore result in a different orientation of the dipole observed following trap pumping. For brevity, we will now refer to each of these configurations as "negative" and "positive" polarities, respectively. So, for this particular scheme, a positively orientated dipole indicates a trapping defect beneath $\phi_4$ while a negatively orientated dipole indicates a trap beneath $\phi_2$.

An additional subtlety is present whereby between clock pulses $t_1$ and $t_2$, and then between $t_3$ and $t_4$, the barrier phase that is biased high is switched. This gives rise to the phenomenon illustrated by Figure 4 whereby the charge storage location shifts by a small amount between each pulse. Taking the example of the transition between $t_1$ and $t_2$; within $t_1$, charge trapping sites beneath the centre and right-hand side of $\phi_2$ become filled, while within $t_2$ charge trapping sites beneath the centre and left-hand side of $\phi_2$ become filled. During $t_2$, charge trapping sites beneath the left-hand side of $\phi_2$ are no longer in the presence of the charge cloud and so are able to emit. The result is a different function for $P_P$ for trapping sites in this location than for the rest of the phase. The exact same logic applies to $\phi_4$ however in this instance trapping sites beneath the right-hand side of $\phi_4$ that exhibit the difference. Of course, the designation of "left hand side" and "right hand side" is dependent upon the signal size and biases used during the trap pumping scheme. For standard bias conditions and a signal level of approximately 10,000 e$^-$, the difference was measured to be $\approx 0.5$ $\mu$m (shown by Figure 4). Thus, following the same analysis presented in [10], for this scheme there are two functions for $P_P$ depending upon the sub-phase location of the defect. For defects located beneath the centre and left hand side of $\phi_2$, and the centre and right hand side of $\phi_4$:

$$I(t_{ph}) = NP_{P1} = NP_c \left( exp(-t_{ph}/\tau_e) - exp(-2t_{ph}/\tau_e) \right) \tag{4.1}$$
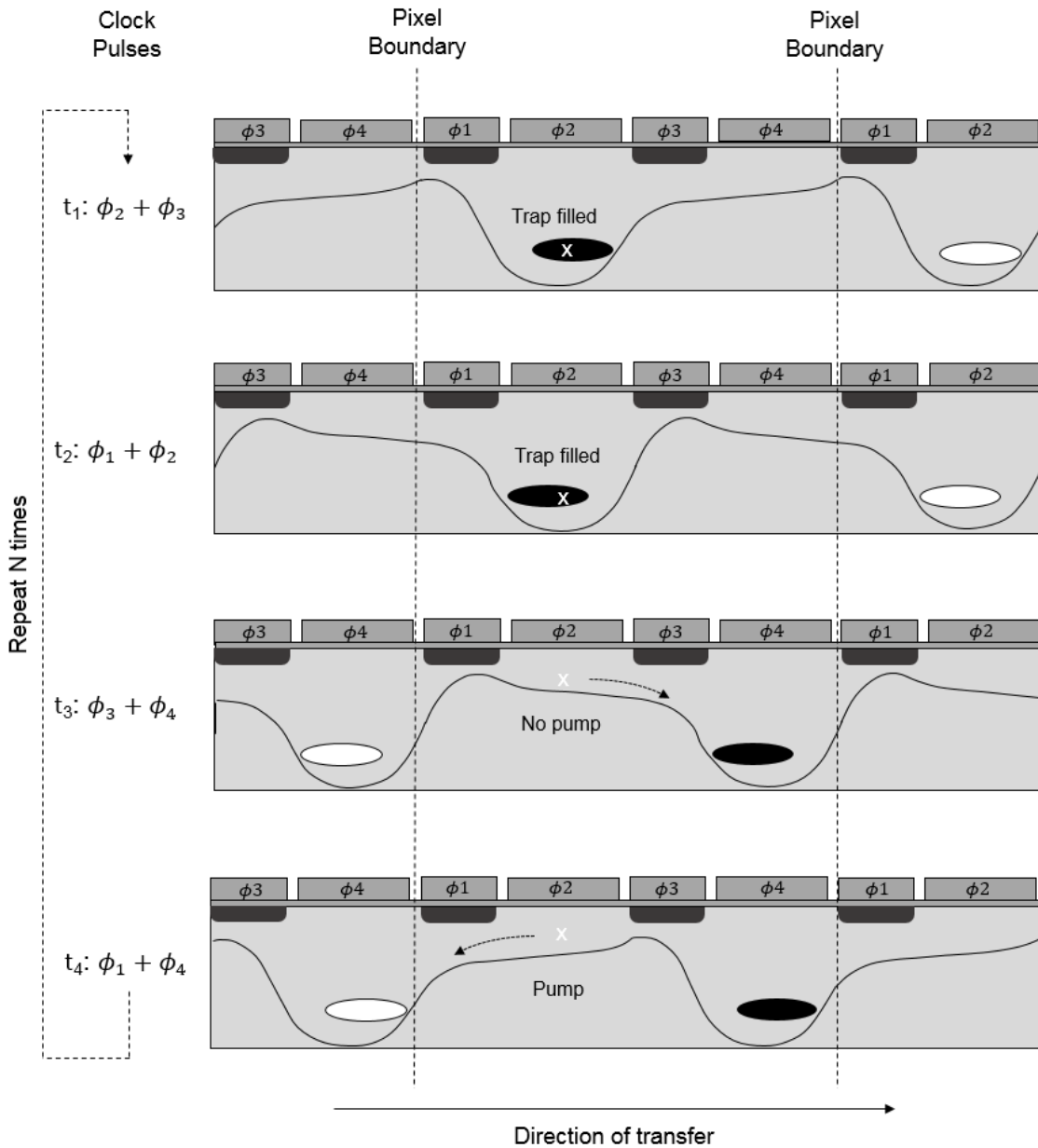
**Figure 6**. Example trap pumping scheme for the 2-phase CCD201. Signal packets are denoted by the shaded ellipses, with the primary (pumped) signal packet illustrated in black and the secondary neighbour packets in white. In this scheme, a total of four separate clock conditions form a complete cycle. The phases in the high level during each stage are labelled on the left, the remaining phases are in the low state. Each clock step is separated by a phase time $t_{ph}$. In the example shown, charge captured beneath the centre of $\phi_2$ can pump against the direction of transfer during clock step 4. The process is repeated N times in order to form dipoles similar to that shown by Figure 1
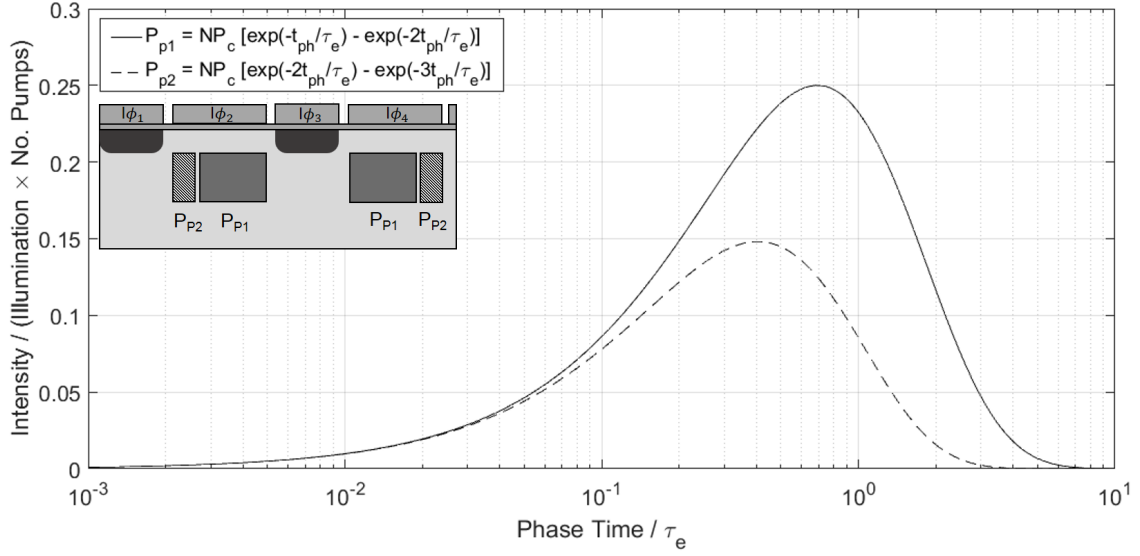
**Figure 7**. Summary of the two functions that describe $P_P$ for the trap pumping scheme shown by Figure 6. Note how each function has a different maximum amplitude and peak location. The internal panel shows a CCD201 image pixel schematic with the physical regions that each function applies to labelled.

Whereas defects beneath the right hand side of $\phi_2$ and the left hand side of $\phi_4$ are described by:

$$I(t_{ph}) = NP_{P2} = NP_c \left(exp(-2t_{ph}/\tau_e) - exp(-3t_{ph}/\tau_e)\right) \tag{4.2}$$

The polarity of the dipole allows one to distinguish between traps beneath $\phi_2$ and $\phi_4$. Figure 7 summarises the analysis for this scheme and shows how each function for $P_p$ differs depending on the location of the defect. We note that in the previous section, the condition for no capture beneath the barrier phases was based upon the regime of smaller signals and short rise times. With the scheme presented in Figure 7, any traps that captured beneath the barrier phases were found to be well described by $P_{P1}$. The example presented here is just one of many trap pumping schemes possible with this architecture of device. As long as the movement of charge can be accurately predicted, one can accurately extract the properties of defects within these devices.

## 5 Experimental verification of trap pumping schemes

One of the primary motivations for the implementation of trap pumping is the increased level of detail concerning individual defects within a pixel that can allow for sophisticated charge correction models and CTI optimisation [5, 13]. Since pre-irradiation trap densities are typically very low, it is primary useful as a technique to help improve the performance of irradiated devices. To validate the technique developed in this study, a selection of CCD201s were irradiated with protons at the Paul Scherrer Institute, Switzerland. The irradiations were performed at room temperature, unbiased and with a 74 MeV primary proton beam. The fluences were normalised to the 10 MeV equivalent

using the Non-Ionising Energy Loss Function (NIEL) described within [24–26], and ranged from 1.0 to 5.0 $\times 10^9$ p/cm$^2$ (10 MeV equiv.).

Approximately half of the parallel section of the devices were irradiated, while the remainder remained shielded. Following irradiation, the trap densities had increased to a level such that the CTI of devices had visibly degraded. To test the trap pumping technique, experimental data was obtained within the parameter space known to contain a defect nominally referred to as the double acceptor state of the silicon divacancy (hereafter VV$^{--}$). A similar study described within [27] was performed on an N-Channel CCD47-10 irradiated at room temperature using 74 MeV protons to a fluence of $2.5 \times 10^9$ protons/cm$^2$ (10 MeV equiv.). The irradiation was performed at the same facility, with the same primary proton beam energy and at the same temperature as this study. The defect energy level and cross section were calculated and found to agree with other literature values for the VV$^{--}$, with an energy level of $(0.240 \pm 0.005)$ eV and a cross section of $1.0 \times 10^{-15}$ cm$^2$. A key conclusion was that there was a large spread in the measured distribution of energy levels and cross sections. This spread was independent of the experimental error, but rather thought to be linked to other factors that could influence the physical properties of each defect, such as orientation within the lattice, proximity to other defects and field enhanced emission [27].

The first step of verification was to validate the results of this study with the results presented in [27], and so data for the defect nominally referred to as the VV$^{--}$ was obtained over the temperature range of 150-200 K in 2 K increments for a CCD201 EMCCD irradiated to $1.0 \times 10^9$ p/cm$^2$ (10 MeV equiv.). This temperature range was chosen since the emission time constant of this trap remained within the limits of the parallel clock driver of the CCD, corresponding to clock times between $10^{-6}$ to $10^{-2}$ s. Measurements of dipole amplitude as a function of phase time ($t_{ph}$) were obtained at each temperature. Trapping sites were identified using a simple thresholding technique, and the correct form of P$_P$ (Equation 4.1 or Equation 4.2) was fitted to each dipole to obtain the emission time constant of each trap. Figure 8 shows an emission time constant histogram obtained at 174 K for both the irradiated and control regions of the device. Within the control region, three distinct peaks are present that were not seen to significantly increase in density following irradiation. Within the irradiated section, a new peak was identified that was not present prior to the irradiation. The location of this peak was consistent with that presented in [27] and nominally identified as the VV$^{--}$, the emission constant histogram from each study is included here as a point of reference.

There are a few notable differences between the two results. Although the primary peak (associated with the VV$^{--}$) is in the same location, the result from [27] shows the peak to be split into two with approximately equal intensity. The result from this study has a small daughter peak at $\approx 10^{-5}$ s however since this co-incides with the location of a defect within the control region each peak is believed to be due to a different defect. We note that in the study presented by [27] used a CCD47-10, with 13 $\mu$m pixels with 3 phases per pixel. The phases within this pixel are asymmetric in width; the first being larger than the remaining two in order to facilitate operation in IMO for some variants. Analysis of the pixel using the methods outlined in the previous section highlighted that this gives rise to 2 functions for $P_p$ for this device, however only one was specified for use using the pumping schemes and analysis routines describes within the study [27]. Analysis of all defects using only one form of $P_p$, namely Equation 4.1, will give rise to the split peak phenomenon since the emission time constant will be incorrect by factor equal to the difference in the peak locations between the correct and incorrect function describing $P_p$.
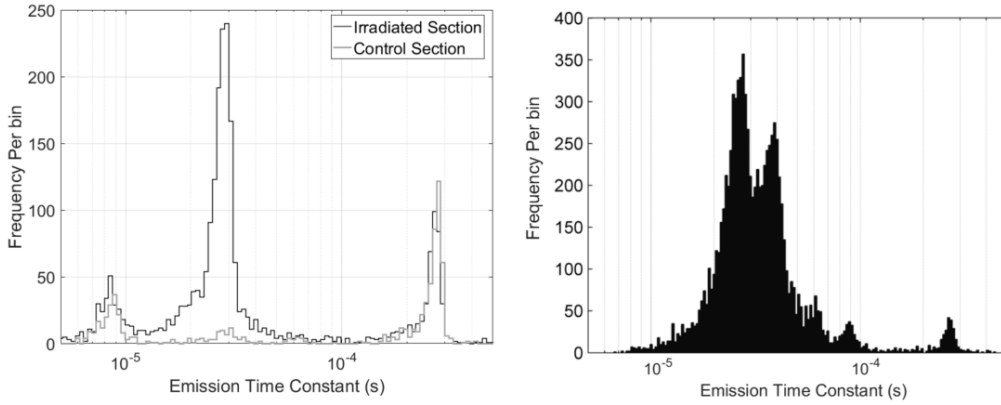
**Figure 8**. Comparison of the results of this study (left) with the results of [27] (right). Data was obtained at 174 K using phase times between $10^{-6}$ s and $10^{-2}$ s

.

To support this hypothesis, the same analysis was performed for the data presented in Figure 8, but this time only Equation 4.1 was used to fit the data. Figure 9 shows the result; note how now a secondary peak has appeared that was not presented in Figure 8. One may note that the intensity of the secondary peak is lower, whereas in [27] the intensity was approximately equal. This is mainly due to the differences in the geometry of pixel phases between the devices used in each study. In this case, traps beneath the left hand side of $\phi_2$ and the right hand side of $\phi_4$ have been incorrectly fitted. The expected difference in the mode value of the emission time constant is expected to be $\approx ln(2) \div ln(3/2) = 1.7$ - very close to the experimentally observed value. Further evidence is given by a histogram showing the fitted values of $P_c$, whereby a secondary peak appears at the expected location of $P_c = 0.6$ that is equal to the factor difference in the max intensity of each form of $P_P$ (Figure 9). A final test was whether CTI measurements correlated with the results returned by trap pumping measurements. Figure 10 shows Extended Pixel Edge Response (EPER [11]) CTI as a function of parallel phase time compared to a emission time constant histogram at the same temperature (174 K). The CTI improves as the phase time is increased beyond the primary peak of the trap histogram. This behaviour is expected since as $t_{ph}$ moves beyond the peak value for $\tau_e$, the majority of the traps are likely to emit charge back into the original signal packet, thus reducing CTI. Based on this analysis, the trap properties returned here are believed to be accurate and coincide with the results of other studies while also explaining the presence of the split peak observed in [27]. With the trap pumping technique validated on the CCD201, we move towards a more detailed discussion concerning the properties of traps identified in this study.
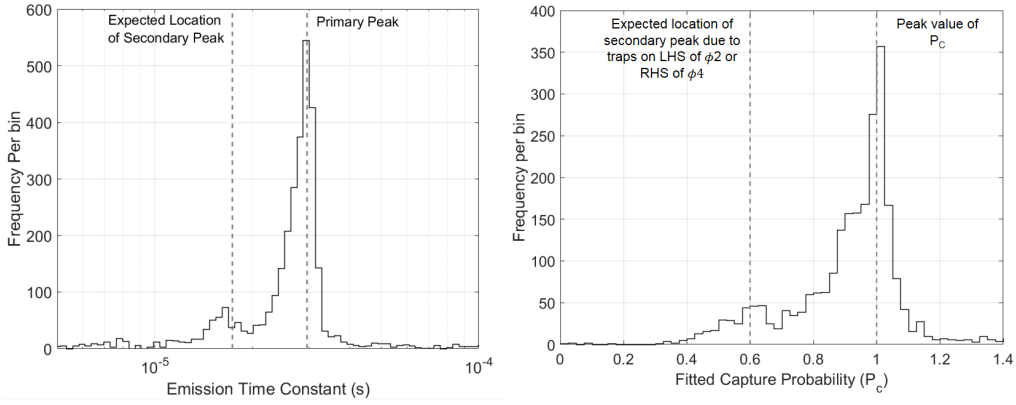
**Figure 9**. Left: Emission time constant histogram obtained at 174 K when only one function is fitted to dipole intensity as a function of phase time ($P_{P1}$). Since dipoles that follow $P_{P2}$ have been incorrectly fitted, a daughter peak appears to the left of the primary peak. The expected theoretical location matches with the measured location. Right: Fitted capture probability ($P_C$) when only $P_{P1}$ is used for analysis. A daughter peak appears at $P_C = 0.6$ due to the difference in peak amplitude between $P_{P1}$ and $P_{P2}$.
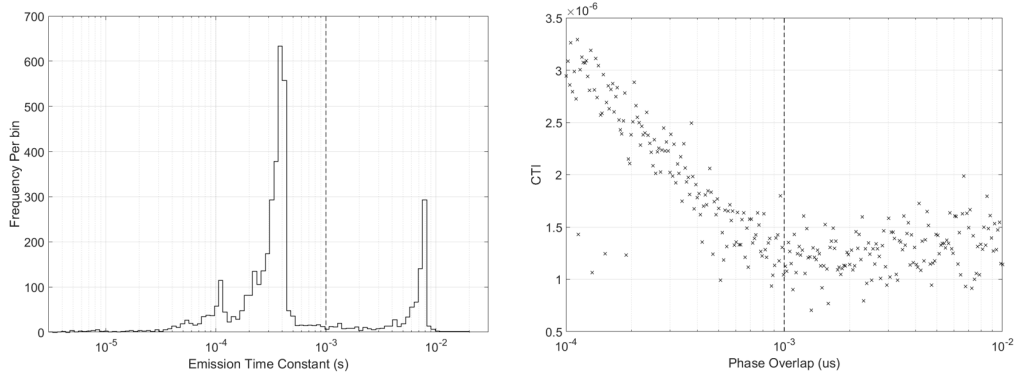


**Figure 10**. Emission time constant histogram obtained at 152 K (left) and CTI measured as a function of phase time using the EPER technique at the same temperature (right). At the position of the dashed line the phase time is long enough such that charge captured by the $VV^{--}$ is emitted back to the parent charge packet. This line therefore corresponds to a minima in the CTI plot.

## 6 Measurement of trap properties

Measurements of the emission time constants of defects in the temperature range of 150-200 K allowed estimation of the trap energy levels and emission cross sections. The trap emission time constant is related to the energy level and cross section through Equation 6 and so measurements of $\tau_e$ as a function of temperature allow derivation of both $E$ and $\sigma$:

$$\tau_e = \sigma v_{th} N_C exp(-E/k_b T) \tag{6.1}$$

where $\sigma$ is the emission cross section, $v_{th}$ is the thermal velocity of the electron, $N_C$ is the electron density of states, E is the trap energy level (eV), T is temperature and $k_b$ is Boltzmann's

constant. Expressions for $v_{th}$ and $N_C$ are given within [10]. Within small temperature ranges, there is a degree of degeneracy between the two parameters, since the same emission cross section at a given temperature can be achieved through variation of either $\sigma$ or E. Therefore, a large temperature range, such as that used in this study, is required to reduce the uncertainty introduced through fitting both parameters.

A total of three separate defect species were identified within the parameter space probed within this study. Two of these species were present prior to the irradiation, and another appeared following the proton irradiation performed at 298 K. The two traps that did not increase due to the irradiation are believed to be due to intrinsic impurities within the device. The mode (peak value) energy levels and cross sections for each identified defect species are summarised within Table 1, alongside a tentative designation of the defect configuration and appropriate literature references. Figure 11 shows a histogram of the energy levels and emission cross sections for each of the defect species for both the control and irradiated regions of the device. There is a large spread in each of the values that is consistent with the spread described in [27]. Analysis of the experimentally derived error highlighted that the spread appears intrinsic to the defects themselves as opposed to error in the experimental determination of these values, as was also seen in [27].

The defects that did not increase due to the irradiation are believed to be related to impurities within the device and dopants introduced during manufacture. For the CCD201, these impurities likely include oxygen and carbon whereas the dopants include phosphorus and boron. Phosphorus-carbon ($C_iP_s$) pairs are known to form within CCDs when irradiated at room temperature where the carbon interstitial ($C_i$) is mobile [28, 29]. A review of the five known possible configurations of this defect is presented within [30] and the ionisation levels listed in Table 1. Within this study, the most prominent defect within the un-irradiated section of the device had an energy level of $E_C$ - 0.32 eV, consistent with the positive charge state of the IIB configuration of the defect [30]. A peak was also present at $E_C$ - 0.23 eV that is consistent with the positive state of the III configuration [30]. We note that the IIA configuration was not present in this dataset at the expected location of $E_C$ - 0.26 eV, with possible reasons for this explained in [28]. Another small peak at 0.27-0.285 eV was identified that may be due to another impurity. A candidate is the $B_iO_i$ defect with a proposed energy level of $E_C$ - 0.27 eV, however the literature value of the cross section [31] does not agree with that found in this study and so this remark remains speculative.

For the irradiated section, the $C_iP_s$ peaks are present at approximately the same intensity as the control region 11. This is an interesting observation, since in principle the irradiation could have liberated more $C_i$ defects that could act to increase the population of $C_iP_s$ pairs [28]. Instead, a single peak appears following irradiation with energy $E_C$ - 0.235 eV that is consistent with the literature value of the double acceptor state of the divacancy [32]. We also note this peak has a mode energy level consistent with positive state of the $C_iP_s$ III defect, however, a plot of defect energy against defect cross section (Figure 11) allowed separation the defects since although the traps share the same energy level they have a different emission cross section. The bottom panel of Figure 11 suggests that the defect introduced by the irradiation is different to the defect identified prior to the irradiation. It is worth explaining that the $VV^{--}$ is not expected to be present prior to irradiation in devices such as these, since the thermal processing during manufacture heats the silicon significantly above the thermal anneal temperature for this defect ($\approx$ 600 K [32]).

The plot of defect energy level against emission cross section revealed a positive correlation

| Trap Species | E - $E_C$ (eV) | $\sigma$ (cm$^2$) | Reference |
|:---:|:---:|:---:|:---:|
| $C_i P_s$ III | $0.230 \pm 0.005$ | $(3.00 \pm 3.00) \times 10^{-15}$ | [30] |
| $C_i P_s$ IIB | $0.310 \pm 0.005$ | $(1.50 \pm 2.00) \times 10^{-14}$ | [30] |
| VV$^{--}$ | $0.235 \pm 0.005$ | $(1.35 \pm 2.00) \times 10^{-15}$ | [27, 32] |

**Table 1**. Summary of the three main trap species identified within the parameter space probed within this study. Two of the traps showed properties consistent with $C_i P_s$ pairs and were present in the device prior to the irradiation. The defect believed to be the VV$^{--}$ appeared following irradiation. The fitted cross sections exhibited large error that was typically comparable to the value itself. The error on cross section was also found to dominate the error on the calculated energy level for each defect.

between the two parameters. The implication is that there is an additional temperature dependence of the cross section that is not accounted for by Equation 6. Literature investigations on similar defects indicate that this may indeed be the case [32] and so future work will entail incorporating this additional dependence to improve the accuracy on derived trap properties. Despite this finding, the mode (peak value) for each trap parameter is believed to be accurate due to the consistency seen with other investigations of a similar nature.

Finally, we note that the combination of temperature (150 to 200 K) and time ($10^{-6}$ to $10^{-2}$ s) space probed in this study limited the minimum and maximum energy level to approximately $E_C$ - 0.2 eV and $E_C$ - 0.3 eV respectively (with dependence on cross section), since at shallower/deeper levels the emission time constant falls outside of the measurement range. The designations described here therefore remain tentative at this time, as a more detailed study that includes measurements at higher temperatures will provide further information concerning the identity of these defects.
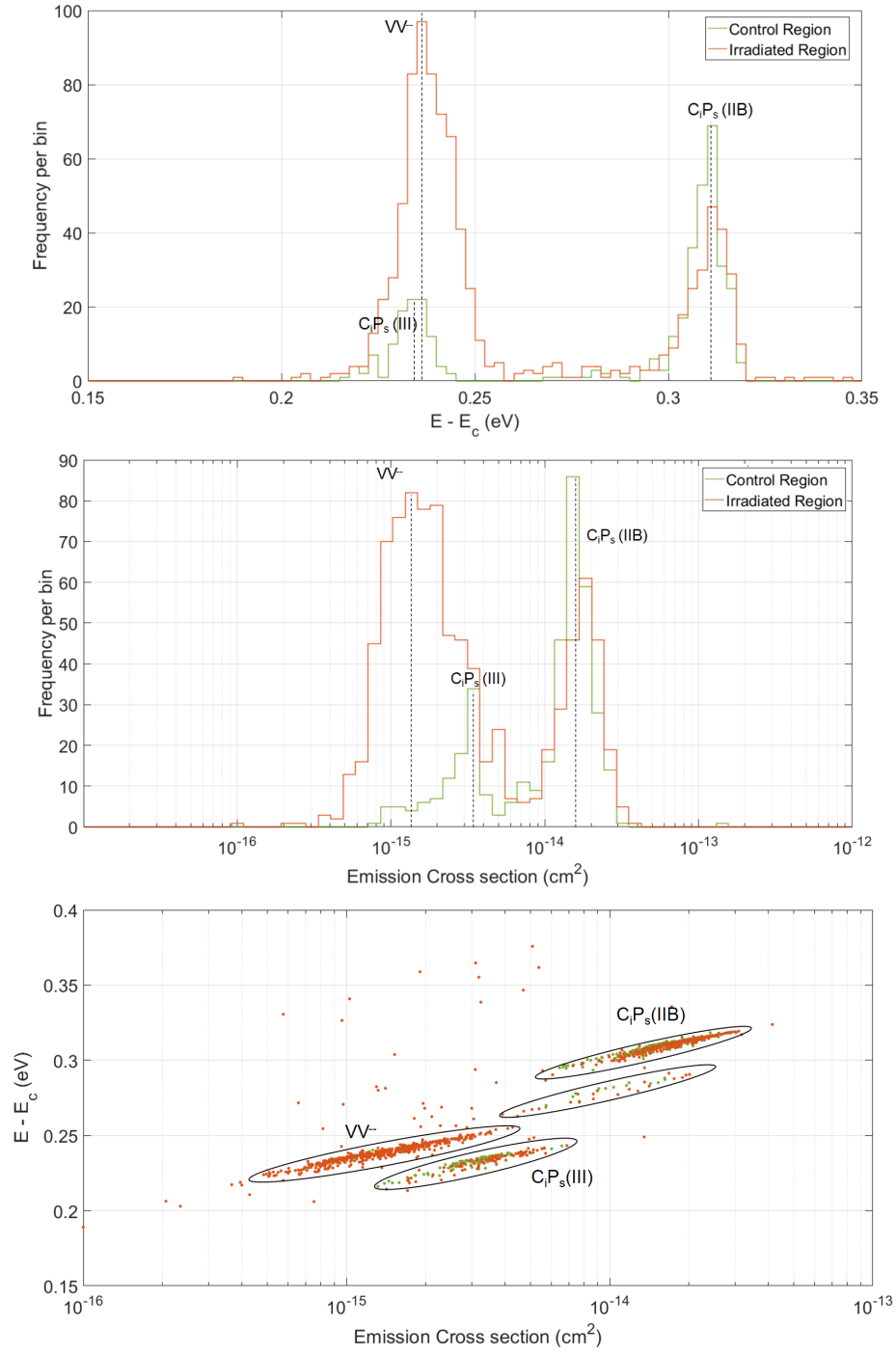
**Figure 11**. Fitted energy levels and cross sections with tentative designations of defect configurations based on the literature sources summarised within Table 1. The plot of energy level against cross section on the lower panel shows how the two defects with energy E ≈ 0.23 eV can be distinguished according to the cross section following irradiation.

# 7 Conclusions

Here we have demonstrated the ability to implement the trap pumping technique on a 2-phase EMCCD. One of multiple possible trap pumping schemes have been presented that provide the capability of sub-phase, sub-micron defect location within a pixel. TCAD simulations highlighted how the exact pixel structure must be well understood in order to accurately extract trap properties from experimental data. The technique has been validated through a brief study into trapping sites within an irradiated CCD201, including traps believed to be the $VV^{--}$ and various configurations of phosphorus-carbon pairs. Comparison of the results from those of a previous study provided largely consistent results, and also explained a "split peak" phenomenon that was previously observed yet not understood. Now that the technique has been validated, the defect parameter space of irradiated devices shall be explored in more detail to provide more information on defects responsible for CTI and improve performance for applications where radiation damage is a key concern.

## Acknowledgments

## References

[1] J. Janesick, T. Elliott and F. Pool, *Radiation damage in scientific charge-coupled devices*, *IEEE Transactions on Nuclear Science* **36** (1989) 572–578.

[2] G. Hopkinson, C. Dale and P. Marshall, *Proton effects in charge-coupled devices*, *IEEE transactions on nuclear science* **43** (1996) 614–627.

[3] N. J. Murray, D. J. Burt, A. D. Holland, K. D. Stefanov, J. P. Gow, C. MacCormick et al., *Multi-level parallel clocking of ccds for: improving charge transfer efficiency, clearing persistence, clocked anti-blooming, and generating low-noise backgrounds for pumping*, in *SPIE Optical Engineering+ Applications*, pp. 88600K–88600K, International Society for Optics and Photonics, 2013.

[4] D. J. Hall, J. Gow, N. J. Murray and A. D. Holland, *Optimization of device clocking schemes to minimize the effects of radiation damage in charge-coupled devices*, *IEEE Transactions on Electron Devices* **59** (2012) 1099–1106.

[5] R. Massey, C. Stoughton, A. Leauthaud, J. Rhodes, A. Koekemoer, R. Ellis et al., *Pixel-based correction for charge transfer inefficiency in the hubble space telescope advanced camera for surveys*, *Monthly Notices of the Royal Astronomical Society* **401** (2009) 371–384.

[6] P. Goudfrooij, R. C. Bohlin, J. Maíz-Apellániz and R. A. Kimble, *Empirical corrections for charge transfer inefficiency and associated centroid shifts for stis ccd observations*, *Publications of the Astronomical Society of the Pacific* **118** (2006) 1455.

[7] K. Dennerl, U. G. Briel, F. Haberl, G. D. Hartner, N. Krause, M. Popp et al., *Determination and correction of the charge transfer efficiency of the pn-ccd camera*, in *EUV, X-Ray, and Gamma-Ray Instrumentation for Astronomy X*, vol. 3765, pp. 232–244, International Society for Optics and Photonics, 1999.

[8] G. Seabroke, A. Holland and M. Cropper, *Modelling radiation damage to esa's gaia satellite ccds*, *arXiv preprint arXiv:0809.0293* (2008) .

[9] J. Skottfelt, D. Hall, J. Gow, N. Murray, A. Holland and T. Prod'homme, *Comparing simulations and test data of a radiation damaged ccd for the euclid mission*, in *SPIE Astronomical Telescopes+ Instrumentation*, pp. 991529–991529, International Society for Optics and Photonics, 2016.

[10] D. J. Hall, N. J. Murray, A. D. Holland, J. Gow, A. Clarke and D. Burt, *Determination of in situ trap properties in ccds using a "single-trap pumping" technique*, *Nuclear Science, IEEE Transactions on* **61** (2014) 1826–1833.

[11] A. Waczynski, E. J. Polidan, P. W. Marshall, R. A. Reed, S. D. Johnson, R. J. Hill et al., *A comparison of charge transfer efficiency measurement techniques on proton damaged n-channel ccds for the hubble space telescope wide-field camera 3*, *IEEE Transactions on nuclear science* **48** (2001) 1807–1814.

[12] G. Y. Prigozhin, S. E. Kissel, M. W. Bautz, C. Grant, B. LaMarr, R. F. Foster et al., *Characterization of the radiation damage in the chandra x-ray ccds*, in *X-ray and Gamma-Ray Instrumentation for Astronomy XI*, vol. 4140, pp. 123–135, International Society for Optics and Photonics, 2000.

[13] N. Murray, A. D. Holland, J. Gow, D. Hall, J. Tutt, D. Burt et al., *Mitigating radiation-induced charge transfer inefficiency in full-frame ccd applications by "pumping" traps*, .

[14] D. Hall, D. Wood, N. Murray, J. Gow, A. Chroneos and A. Holland, *In situ trap properties in ccds: the donor level of the silicon divacancy*, *Journal of Instrumentation* **12** (2017) P01025.

[15] N. J. Mostek, C. J. Bebek, A. Karcher, W. F. Kolbe, N. A. Roe and J. Thacker, *Charge trap identification for proton-irradiated p+ channel ccds*, in *Proc. SPIE*, vol. 7742, p. 774216, 2010.

[16] D. Wood, D. Hall, N. Murray, J. Gow, A. Holland, P. Turner et al., *Studying charge-trapping defects within the silicon lattice of a p-channel ccd using a single-trap "pumping" technique*, *Journal of Instrumentation* **9** (2014) C12028.

[17] L. K. Harding, R. T. Demers, M. Hoenk, P. Peddada, B. Nemati, M. Cherng et al., *Technology advancement of the ccd201-20 emccd for the wfirst coronagraph instrument: sensor characterization and radiation damage*, *Journal of Astronomical Telescopes, Instruments, and Systems* **2** (2016) 011007–011007.

[18] H. Michaelis, T. Behnke, S. Mottola, A. Krimlowski, B. Borgs, A. Holland et al., *Investigations on performance of electron multiplied ccd detectors (emccds) after radiation for observation of low light star-like objects in scientific space missions*, in *Sensors, Systems, and Next-Generation Satellites XVII*, vol. 8889, p. 88891D, International Society for Optics and Photonics, 2013.

[19] P. Jerram, P. J. Pool, R. Bell and D. J. e. a. Burt, *The llccd: low-light imaging without the need for an intensifier*, vol. 4306, pp. 178–186, 2001. DOI.

[20] M. S. Robbins and B. J. Hadwen, *The noise performance of electron multiplying charge-coupled devices*, *Electron Devices, IEEE Transactions on* **50** (2003) 1227–1232.

[21] SILVACO, *SILVACO ATLAS's User Manual Device Simulation Software*.

[22] e2v technologies, *e2v ccd201-20 datasheet*, .

[23] N. Bush, K. Stefanov, D. Hall, D. Jordan and A. Holland, *Simulations of charge transfer in electron multiplying charge coupled devices*, *Journal of Instrumentation* **9** (2014) C12042.

[24] E. Burke et al., *Energy dependence of proton-induced displacement damage in silicon*, *Nuclear Science, IEEE Transactions on* **33** (1986) 1276–1281.

[25] V. A. Van Lint, *The physics of radiation damage in particle detectors*, *Nuclear Instruments and*

*Methods in Physics Research Section A: Accelerators, Spectrometers, Detectors and Associated Equipment* **253** (1987) 453–459.

[26] J. Srour, C. J. Marshall and P. W. Marshall, *Review of displacement damage effects in silicon devices*, *Nuclear Science, IEEE Transactions on* **50** (2003) 653–670.

[27] D. Wood, D. Hall, J. Gow and A. Holland, *A study of the double-acceptor level of the silicon divacancy in a proton irradiated n-channel ccd*, *SPIE Proceedings: High Energy, Optical, and Infrared Detectors for Astronomy VII* **9915** (2016) .

[28] M. Bautz, G. Prigozhin, S. Kissel, B. LaMarr, C. Grant and S. Brown, *Anomalous annealing of a high-resistivity ccd irradiated at low temperature*, *IEEE transactions on nuclear science* **52** (2005) 519–526.

[29] C. Grant, B. LaMarr, G. Prigozhin, S. Kissel, S. Brown and M. Bautz, *Physics of reverse annealing in high-resistivity chandra acis ccds*, *arXiv preprint arXiv:0807.1721* (2008) .

[30] E. Gürer, B. W. Benson and G. D. Watkins, *Configurational metastability of carbon-phosphorus pair defects in silicon*, in *Materials Science Forum*, vol. 83, pp. 339–344, Trans Tech Publ, 1992.

[31] J. Schmidt, C. Berge and A. G. Aberle, *Injection level dependence of the defect-related carrier lifetime in light-degraded boron-doped czochralski silicon*, *Applied physics letters* **73** (1998) 2167–2169.

[32] A. Hallén, N. Keskitalo, F. Masszi and V. Nágl, *Lifetime in proton irradiated silicon*, *Journal of Applied Physics* **79** (1996) 3906–3914.